

Off-Line Efficiency Mapping of Induction Motors Operated in Wide Torque-Speed Ranges

Original

Off-Line Efficiency Mapping of Induction Motors Operated in Wide Torque-Speed Ranges / Stiscia, Ornella; Rubino, Sandro; Vaschetto, Silvio; Cavagnino, Andrea; Tenconi, Alberto. - ELETTRONICO. - (2020), pp. 1075-1082. (2020 IEEE Energy Conversion Congress and Exposition (ECCE) Detroit, MI, USA, USA 11/10/2020 - 15/10/2020) [10.1109/ECCE44975.2020.9236081].

Availability:

This version is available at: 11583/2854341 since: 2021-02-11T10:15:16Z

Publisher:

IEEE

Published

DOI:10.1109/ECCE44975.2020.9236081

Terms of use:

This article is made available under terms and conditions as specified in the corresponding bibliographic description in the repository

Publisher copyright

IEEE postprint/Author's Accepted Manuscript

©2020 IEEE. Personal use of this material is permitted. Permission from IEEE must be obtained for all other uses, in any current or future media, including reprinting/republishing this material for advertising or promotional purposes, creating new collecting works, for resale or lists, or reuse of any copyrighted component of this work in other works.

(Article begins on next page)

Off-Line Efficiency Mapping of Induction Motors Operated in Wide Torque-Speed Ranges

Ornella Stiscia, *Student Member, IEEE*

Politecnico di Torino
Dipartimento Energia
Torino, Italy
ornella.stiscia@polito.it

Sandro Rubino, *Member, IEEE*

Politecnico di Torino
Dipartimento Energia
Torino, Italy
sandro.rubino@polito.it

Silvio Vaschetto, *Senior Member, IEEE*

Politecnico di Torino
Dipartimento Energia
Torino, Italy
silvio.vaschetto@polito.it

Andrea Cavagnino, *Fellow, IEEE*

Politecnico di Torino
Dipartimento Energia
Torino, Italy
andrea.cavagnino@polito.it

Alberto Tenconi, *Senior Member, IEEE*

Politecnico di Torino
Dipartimento Energia
Torino, Italy
alberto.tenconi@polito.it

Abstract— In the context of a progressive component virtualization for energetic assessments in variable speed and load operations, this paper presents a methodology for computing the efficiency maps of three-phase induction motors. The proposed approach is based on the conventional machine equivalent circuit to quickly obtain a set of efficiency maps at different machine temperatures and supply voltage levels. The well-known no-load and locked-rotor tests are used to determine the motor parameters at different frequencies and voltages, taking into account the machine nonlinearities and the iron losses. The approach has been validated on an 11 kW, 4 poles, 50 Hz induction motor tested in different operating conditions.

Keywords— *induction motor, efficiency maps, locked-rotor test, no-load test, iron losses, magnetic saturation, virtualization.*

I. INTRODUCTION

In the energy transition pathway towards more efficient and carbon-free solutions, the electrification of a wide range of applications represents a sustainable way to achieve these goals [1]. This paradigm shift involves a substantial redesign of several already engineered systems, and their accurate energetic assessment is of primary importance [2]-[4]. From an engineering standpoint, components virtualization is a sustainable approach to perform comprehensive simulations of complex systems, also considering variable load profiles [5]. This allows markedly reducing the need for expensive and time consuming testing activities. Focusing on electrical machines, different virtualization alternatives can be considered depending on the required outputs and modeling constraints, such as simulation time and accuracy [6]. For energetic evaluations, models based on machine losses and efficiency usually represent the most convenient solution [7]. Different complexity levels can be considered for the energetic model depending on the load profile. For a fixed working point, a constant efficiency value can conveniently represent the components' energetic behavior. However, for variable operations in wide torque-speed ranges, an approach based on efficiency maps is usually adopted [8], [9].

Induction motor (IM) manufacturers usually provides efficiency information only for few working points. Rarely they provide efficiency maps. Moreover, even if efficiency maps are provided, they are typically referred to a specific machine temperature and for a defined supply voltage. While this level of information may be sufficient for machines operated at fixed working point, it may not be enough accurate when variable operations in wide torque-speed ranges are considered. Indeed, in these cases the terminal voltage as well as the machine temperature can assume very different values in function of the required torque and speed profiles.

This paper presents a methodology for computing efficiency maps of three-phase induction motors for different machine temperature and supply voltage values. In detail, the proposed approach is based on the IM equivalent circuit, which parameters can be easily obtained by the conventional no-load and locked-rotor tests executed at the different voltages and frequencies of interest. The sets of machine parameters measured at the different voltage and frequency levels allow modeling the effects of the magnetic saturation and iron losses for all the working points in the torque/speed plane. Then, multiple efficiency maps are obtained solving the equivalent circuit in steady-state conditions, considering the temperature impacts on the stator and rotor resistances. The analytical model has been developed in rotor flux-oriented (d,q) coordinates, and includes the determination of the maximum-torque per ampere (MTPA) and maximum-torque per voltage (MTPV) profiles, as well as the maximum torque per speed profile (MTPS) achievable for the different supply voltages [10].

The proposed method does not require a dedicated test rig or a climatic chamber for the experimental activity. Indeed, the no-load and locked-rotor tests for the measurements of the equivalent circuit parameters are executed at ambient temperature without mounting the machine on a test bench [11], [12]. Besides the reduced test setup complexity, this approach also saves the time required for the machine thermal stabilization if the efficiency had to be measured at different temperatures. Since the parameters required as input by the proposed procedure can be easily measured, detailed information about the design data of the electrical machine, such as dimensions, winding specifications, etc. are not required. If these data are available, the parameters of the IM equivalent circuit could also be estimated replicating the no-load and locked-rotor tests by analytical or finite element analyses. Obviously, also the complete set of efficiency maps might be obtained through numerical simulations, but at the cost of burdensome computational times, in particular, if FEM three-dimensional models are used [13]-[15].

As the electromagnetic and the thermal time constants under variable speed/load profiles are substantially different, the proposed approach has been conceived for computing the IM efficiency maps in 'off-line' with respect to the comprehensive system simulations. This paper reports step-by-step the proposed mapping methodology and its validation using an 11 kW, 4 poles, 50 Hz squirrel cage induction motor. The efficiency maps for different operating conditions have been computed by the algorithm using the measured machine parameters as input data. The obtained results are compared with measurements conducted on the machine in load conditions.

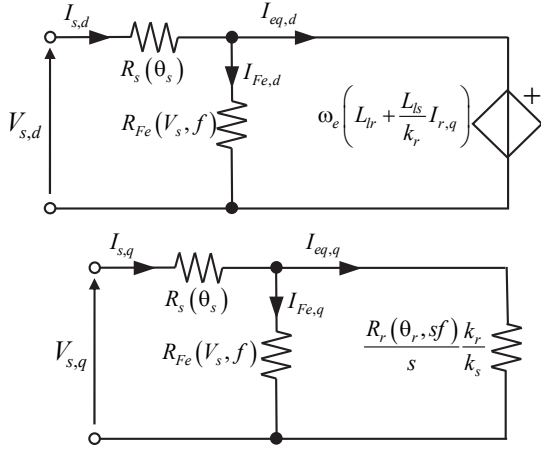


Fig. 1: Induction machine steady-state equivalent circuit in rotor flux-oriented (d, q) coordinates.

II. INDUCTION MACHINE MODELING

The proposed efficiency mapping consist of an analytic model based on the IM equivalent circuit in rotor flux-oriented (d, q) coordinates [16]. In detail, d -axis corresponds to the position of the rotor flux linkage vector. Thus, the electromagnetic behavior of the machine in steady-state conditions can be expressed as in (1), where $\bar{V}_{s,dq}$, $\bar{\Lambda}_{s,dq}$, and $\bar{I}_{eq,dq}$ are the stator voltage vector, stator flux linkage vector, and equivalent current vector, respectively.

$$\begin{cases} \bar{V}_{s,dq} = R_s \cdot \bar{I}_{eq,dq} + \left(1 + \frac{R_s}{R_{Fe}}\right) \cdot j \cdot \omega_e \cdot \bar{\Lambda}_{s,dq} \\ 0 = \frac{R_r}{s} \cdot \bar{I}_{r,dq} + j \cdot (\omega_e - p \cdot \omega_r) \cdot \bar{\Lambda}_{r,dq} \\ \bar{\Lambda}_{s,dq} = \sigma L_s \cdot \bar{I}_{eq,dq} + k_r \cdot \bar{\Lambda}_{r,dq} \\ \bar{\Lambda}_{r,dq} = L_m \cdot (I_{eq,d} + j \cdot 0) \end{cases} \quad (1)$$

The use of the equivalent current vector $\bar{I}_{eq,dq}$ allows separating the portion of stator current that is directly related to the flux- and torque- productions from that related to the iron losses. The rotor quantities in terms of flux linkage vector $\bar{\Lambda}_{r,dq}$ and current vector $\bar{I}_{r,dq}$ are reported to the stator. The mechanical and synchronous speeds are indicated with ω_r and ω_e . Finally, the variable s denotes the slip. Concerning the IM parameters, R_s , R_{Fe} , and R_r stand for the stator resistance, the equivalent resistance of the iron losses, and rotor resistance (referred to the stator), respectively. The stator inductance and the magnetizing inductance are denoted with L_s and L_m . The rotor coupling factor and the total leakage coefficient are denoted with k_r and σ , respectively. Finally, p stands for the pole pairs of the machine.

The equation system in (1) leads to the equivalent circuit shown in Fig. 1, where k_s stands for the stator coupling factor, while L_{ls} and L_{lr} are the stator and rotor leakage inductances, respectively. It is important to remark that the proposed approach does not consider constant machine parameters. Therefore, the equivalent circuit in Fig. 1 highlights the variations of R_{Fe} on the frequency f and supply voltage V_s , as well as the dependency of the stator and rotor resistances on the respective temperatures (i.e. θ_s and θ_r). Moreover, the model also considers the dependency of the rotor resistance on the slip frequency sf , as well as the contribution of the stator leakage fluxes to the iron losses [17].

Although it is not directly shown in Fig. 1, the effect of the magnetic saturation on both the coupling factors of stator k_s and rotor k_r and total leakage coefficient σ , is included. Indeed, such parameters are computed as shown in (2).

$$\begin{aligned} k_s(I_{eq,d}) &= \frac{L_m(I_{eq,d})}{L_m(I_{eq,d}) + L_{ls}} = \frac{L_m(I_{eq,d})}{L_s(I_{eq,d})} \\ k_r(I_{eq,d}) &= \frac{L_m(I_{eq,d})}{L_m(I_{eq,d}) + L_{lr}} = \frac{L_m(I_{eq,d})}{L_r(I_{eq,d})} \\ \sigma &= 1 - k_s(I_{eq,d}) \cdot k_r(I_{eq,d}) \end{aligned} \quad (2)$$

In (2), it is remarked the dependency of the magnetizing inductance L_m on the d -axis component of the equivalent current. In other words, this current assumes the meaning of magnetizing current when the IM model in rotor flux-oriented (d, q) coordinates is considered.

Once the parameters of the equivalent circuit are determined for the different supply voltages, frequencies and working temperatures, the machine loss components can be reasonably computed for the different working points in the complete torque-speed range. In detail, the stator and rotor Joule losses are computed considering the impact of the machine temperature and frequency on the resistances, while the iron losses are calculated considering the magnetic circuit loading, including the saturation. The additional stray load losses of the machine can be considered as a percentage of the actual mechanical power, as also suggested by international Standards for some IM efficiency test methods [11], [12]. Therefore, by the power balance applied to the IM model in (1), the electromagnetic torque is computed as in (3).

$$T_{em} = \frac{3}{2} \cdot p \cdot (\Lambda_{s,d} \cdot I_{eq,q} - \Lambda_{s,q} \cdot I_{eq,d}) \quad (3)$$

$$T_{shaft} = T_{em} \mp T_{fw}(\omega_r) \quad (4)$$

Including in the power balance the friction & windage losses, hereafter denoted with T_{fw} , the net torque at the machine shaft T_{shaft} is computed by (4), where the minus is used for motor operations, while the sum for generator mode. It has been highlighted the dependency of the friction effects on the mechanical rotor speed ω_r .

III. MEASUREMENT OF THE MODEL PARAMETERS

According to the IM modeling (1)–(4), the proposed mapping approach requires in input the equivalent circuit parameters which can be obtained by performing the no-load and locked-rotor tests in accordance to the standard procedures, supplying the machine at different frequency levels [11], [12].

In particular, for each supply frequency, the different voltage levels applied during the tests allow defining a set of values for the magnetizing inductance in function of the equivalent magnetizing current $L_m(I_{eq,d})$, a set of values for the iron resistance in function of the supply voltage and frequency $R_{Fe}(V_s, f)$. The no-load tests also allow modeling the mechanical losses $P_{fw}(f)$ with a polynomial function of the synchronous speed or the frequency. On the other hand, the locked-rotor test performed at a reduced supply voltage allows defining the leakage inductances. This test, executed at different frequencies, allows taking into account the skin effect on the stator and rotor resistances.

TABLE I
MAIN DATA FOR THE IM UNDER TEST

Pole count	4
Rated power	11 kW
Rated speed	1440 rpm
Rated rms voltage	400 V/230 V
Rated rms current	21.5 A/37.5 A
Rated frequency	50 Hz
Connection	star/delta

TABLE II
EQUIVALENT CIRCUIT PARAMETERS MEASURED FOR THE IM UNDER TEST AT THE RATED FLUX AND RATED FREQUENCY

Stator resistance $R_s @ \theta_s = 75^\circ\text{C}$	295 m Ω
Rotor resistance $R_r @ \theta_r = 75^\circ\text{C}$	454 m Ω
Iron loss resistance R_{Fe}	500 Ω
Magnetizing inductance L_m	77 mH
Stator leakage inductance L_{ls}	2.7 mH
Rotor leakage inductance L_{lr}	3.9 mH

Note that, the temperature effect on the stator and rotor resistances is taken into account through the resistivity variation coefficients in the data post-elaboration in the mapping algorithm.

A. Parameter measurements for the machine under test

The main data for the Total Enclosed Fan Cooled (TEFC) induction motor considered for the validation of the proposed mapping procedure are listed in Table I.

The no-load and locked-rotor tests for the determination of the sets of equivalent circuit parameters have been done supplying the machine with a sinusoidal power supply in the frequency range 30 Hz – 80 Hz. Table II summarizes the measured parameters at the rated supply voltage and frequency, and the conventional temperature of 75 °C.

The variation of the iron loss resistance R_{Fe} versus the stator voltage for the different supply frequencies is shown in Fig. 2, where the black markers represent the measured points. This figure shows that, increasing the voltage level, R_{Fe} increases smoothly until the rated flux is achieved; beyond these values the iron loss resistance slightly reduces again because of the iron losses increase. As expected, Fig. 2 also shows that as the ratio V_s/f increases, the iron resistance decreases, leading to higher losses.

The magnetizing inductance versus the no-load current is shown in Fig. 3. It should be noted that in no-load conditions, the no-load current practically corresponds to the equivalent d -axis current ($I_{eq,d}$) due to the low impact of the $P_{Fe} + P_{fw}$ losses. The figure also well shows the saturation phenomenon in the machine magnetic circuit for high magnetizing currents. Finally, Fig. 4 shows the friction & windage torque as a function of the shaft speed ω_r . The obtained parabolic trend has been determined extrapolating at zero speed the curves of the no-load powers measured at the different supply voltages and frequencies.

IV. THE MAPPING ALGORITHM

The proposed mapping algorithm is structured in five subsequent steps, as schematically shown in the flow diagram in Fig. 5 and thoroughly described hereafter.

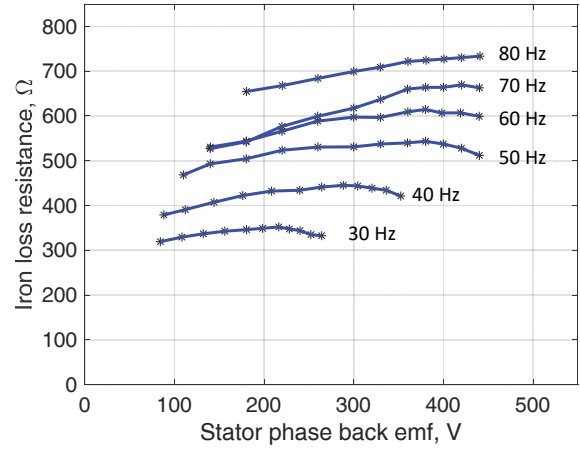


Fig. 2: Iron loss resistance R_{Fe} vs. the stator phase back-emf measured for the machine under test at different supply frequencies (star connection).

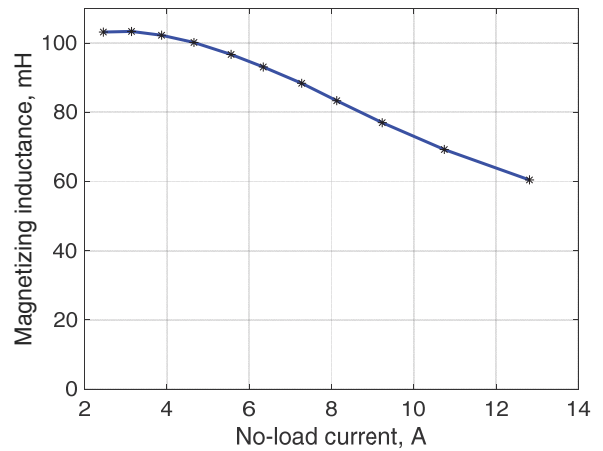


Fig. 3: Magnetizing inductance vs. no-load rms current measured for the machine under test (star connection).

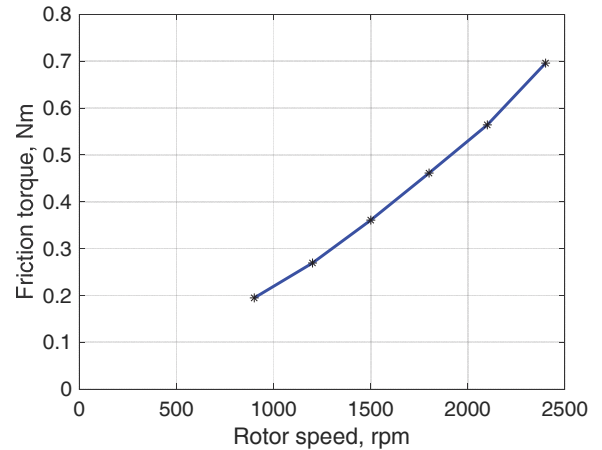


Fig. 4: Friction & windage torque vs. the speed for the machine under test.

A. Step 1: Flux & Current maps

The evaluation of each electromagnetic quantity (flux, voltage, current) is performed on a predefined equivalent (d, q) current map $\bar{I}_{eq,dq}^{map}$, whose limits depend on the maximum magnetizing current $I_{eq,d-max}$, and the maximum phase current I_{max} . The first limit is related to the maximum allowed magnetizing current I_{m-max} , while the second one usually corresponds to the current constraint of the motor – supply system.

Therefore, the equivalent current map in (d,q) coordinates consists of a regular grid, whose step ΔI is selected according to the desired resolution, and the current limits are computed as in (5).

$$d - axis : \begin{cases} I_{eq,d-\min} = 0 \\ I_{eq,d-\max} = I_{m-\max} \end{cases} \quad (5)$$

$$q - axis : \begin{cases} I_{eq,q-\min} = -\sqrt{I_{\max}^2 - I_{eq,d-\max}^2} \\ I_{eq,q-\max} = +\sqrt{I_{\max}^2 - I_{eq,d-\max}^2} \end{cases}$$

Combining the IM model in (1) with the variable magnetizing inductance $L_m(I_{eq,d})$ obtained from the no-load tests (Fig. 3), the stator fluxes are computed for each point of the equivalent current map. Therefore, the stator (d,q) flux maps $\Lambda_{s,d}^{map}$, $\Lambda_{s,q}^{map}$ are computed as shown in (6).

$$\begin{cases} \Lambda_{s,d}^{map} = L_s^{map}(I_{eq,d}) \cdot I_{eq,d}^{map} \\ \Lambda_{s,q}^{map} = \sigma^{map}(I_{eq,d}) \cdot L_s^{map}(I_{eq,d}) \cdot I_{eq,q}^{map} \end{cases} \quad (6)$$

In (6), L_s^{map} and σ^{map} are the maps of the stator inductance and the total leakage factor. It is important to highlight that the ‘.’ and ‘/’ operators between two maps corresponds to element-wise products and division between matrices, respectively. In accordance to (3), once the maps for the equivalent currents and stator fluxes are obtained, the map for the electromagnetic torque is T_{em}^{map} computed by (7), both for motoring and generator mode.

$$T_{em}^{map} = \frac{3}{2} \cdot p \cdot (\Lambda_{s,d}^{map} \cdot I_{eq,q}^{map} - \Lambda_{s,q}^{map} \cdot I_{eq,d}^{map}) \quad (7)$$

B. Step 2: Electrical and mechanical variables computation

At this step, the proposed mapping approach requires the computation of all the electrical and mechanical quantities in the complete speed range using the flux and current maps previously computed. For this purpose, the maps for the slip speeds in the different working points are firstly computed by (8), where L_r^{map} are the maps of the rotor inductance, whose values depend on the equivalent d -axis current and rotor frequency. The set of values for the rotor resistances is obtained referring the measured value at the different rotor temperatures considered for the analysis.

$$\omega_{slip}^{map} = \frac{L_r^{map}(I_{eq,d})}{R_r(\theta_r)} \cdot I_{eq,q}^{map} / I_{eq,d}^{map} \quad (8)$$

Therefore, for each electrical pulsation ω_e that supplies the machine in the speed range from 0 up to the maximum speed, the map of the mechanical speed ω_r^{map} is computed by (9), where ω_{slip} is negative for generator mode.

$$\omega_r^{map} = \omega_e^{map} - \omega_{slip}^{map} \quad (9)$$

Hence, for each mechanical speed, the mechanical net torque can be computed subtracting from the electromagnetic torque the friction & windage component determined by tests (Fig. 4):

$$T_{shaft}^{map} = T_{em}^{map} \mp T_{fw}^{map} \quad (10)$$

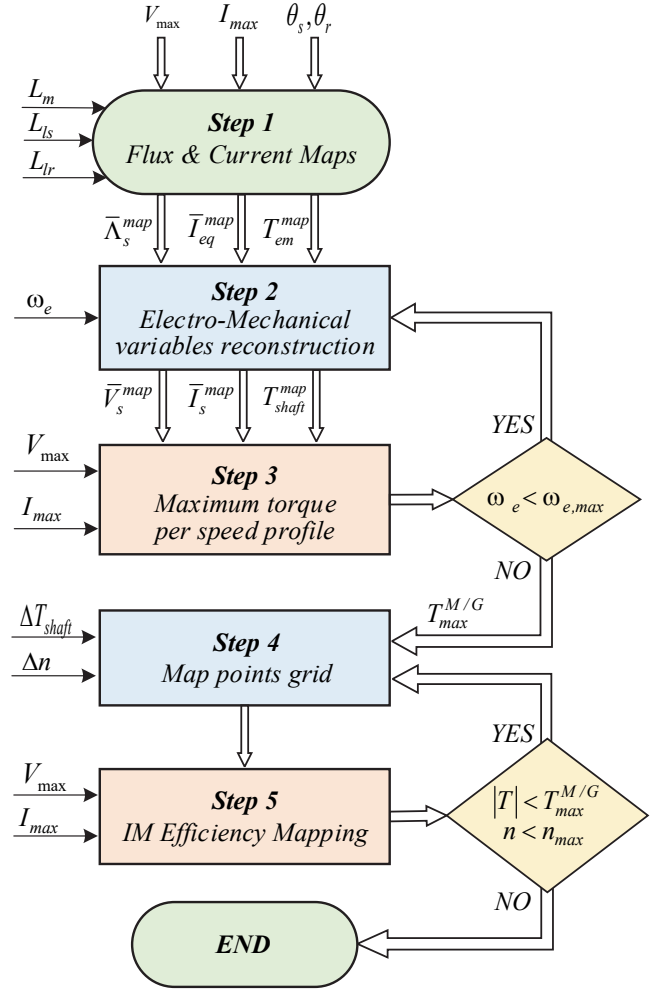


Fig. 5: Flow diagram of the proposed efficiency mapping.

For each ω_e value, the back-emf can be computed by the stator (d,q) fluxes:

$$E_s^{map} = \omega_e \cdot \sqrt{\Lambda_{s,d}^{map} \cdot \Lambda_{s,d}^{map} + \Lambda_{s,q}^{map} \cdot \Lambda_{s,q}^{map}} \quad (11)$$

When E_s^{map} and the supply frequency are known, the iron loss resistance R_{Fe}^{map} can be extracted by the experimental measurements (see Fig. 2). Finally, the maps of the stator voltages and the stator currents, can be computed as specified in (12) and (13), respectively.

$$\begin{cases} V_{s,d}^{map} = R_s(\theta_s) \cdot I_{eq,d}^{map} - \omega_e \cdot \Lambda_{s,q}^{map} - \omega_e \cdot R_s(\theta_s) \cdot \Lambda_{s,q}^{map} / R_{Fe}^{map} \\ V_{s,q}^{map} = R_s(\theta_s) \cdot I_{eq,q}^{map} + \omega_e \cdot \Lambda_{s,d}^{map} + \omega_e \cdot R_s(\theta_s) \cdot \Lambda_{s,d}^{map} / R_{Fe}^{map} \\ V_s^{map} = \sqrt{V_{s,d}^{map} \cdot V_{s,d}^{map} + V_{s,q}^{map} \cdot V_{s,q}^{map}} \end{cases} \quad (12)$$

$$\begin{cases} I_{s,d}^{map} = I_{eq,d}^{map} - \omega_e \cdot \Lambda_{s,q}^{map} / R_{Fe}^{map} \\ I_{s,q}^{map} = I_{eq,q}^{map} + \omega_e \cdot \Lambda_{s,d}^{map} / R_{Fe}^{map} \\ I_s^{map} = \sqrt{I_{s,d}^{map} \cdot I_{s,d}^{map} + I_{s,q}^{map} \cdot I_{s,q}^{map}} \end{cases} \quad (13)$$

C. Step 3: Maximum-torque per speed profile

At this step, for each speed value, the working points that overcome the current and voltage limits of the machine or supply power converter must be ruled out by the maps. Therefore, the developed mapping algorithm considers only the working points that satisfy the following constraints:

$$\begin{cases} V_s = \sqrt{V_{s,d}^2 + V_{s,q}^2} \leq \sqrt{2}V_{\max} \\ I_s = \sqrt{I_{s,d}^2 + I_{s,q}^2} \leq I_{\max} \end{cases} \quad (14)$$

where V_{\max} represents the sinusoidal voltage limit for the supply and, as aforementioned, I_{\max} is the amplitude limit of the phase current for the motor – supply system.

This results in the computation of the maximum torque per speed (MTPS) profiles at the different supply voltages and machine operating temperatures considered in the analysis. In detail, the MTPS consists of finding the maximum (motoring) and minimum (generator) shaft torques for each mechanical speed. Examples of MTPS profiles computed by the mapping are shown in Fig 6 and in Fig. 7. In particular, Fig. 6 has been obtained considering a constant temperature value equal to 25 °C both for the stator and the rotor, and two different values of the maximum rms phase voltage.

Obviously, the available maximum voltage strongly affects the MTPS profiles, markedly reducing the base speed at which the flux weakening operation occurs, thus reducing the MTPA operation of the machine. Moreover, it is noted how in generation mode, the flux weakening occurs for a speed value higher than in motoring mode. This difference is related to the sign change of both the slip speed and the voltage drops on the stator resistances. However, the sign-changing of the slip speed has a higher impact since it leads to a lower amplitude of the stator voltages for a given amplitude of the stator flux linkage. Finally, it is noted how for low values of the maximum supply voltage, the MTPV operation starts in the low/medium speed range of the machine.

On the other hand, Fig. 7 shows examples of MTPS profiles computed considering a maximum rms voltage equal to 250 V, and variable stator and rotor temperatures. Please note that these results have been obtained considering the same temperature values both for the stator and the rotor parts. However, it has been found that the temperature increase marginally impacts the MTPS profile, slightly reducing the base speed at which the flux weakening region starts. This is caused by the increment of the voltage drop on the stator resistance with the temperature.

D. Step 4: Map points grid

Once the MPTS profiles have been determined, it is possible to define the working points in the torque-speed plane where the efficiency values have to be computed. The number of points per map depends on the selected resolutions in terms of torque (ΔT_{shaft}) and speed (Δn) steps. These values have to be accurately selected as a compromise between efficiency maps resolution and computational time required for the step 5 execution. Figure 8 shows an example of an efficiency map point grid for defined MTPS profiles in motor and generator operations.

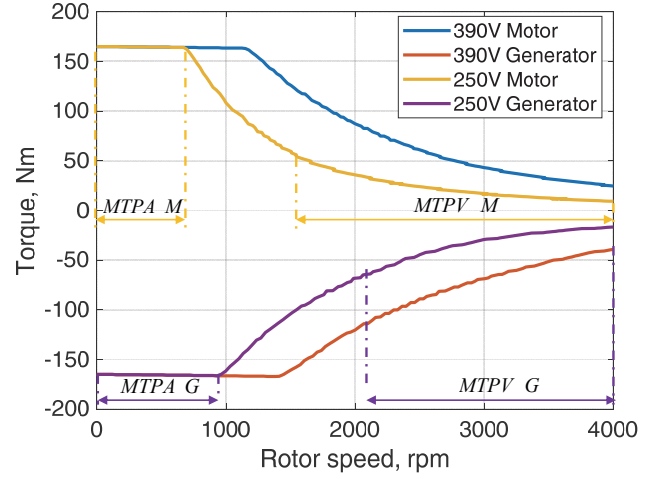


Fig. 6: Example of MTPS profiles computed at different dc-link voltages and fixed stator and rotor temperatures ($\theta_s = \theta_r = 25^\circ\text{C}$).

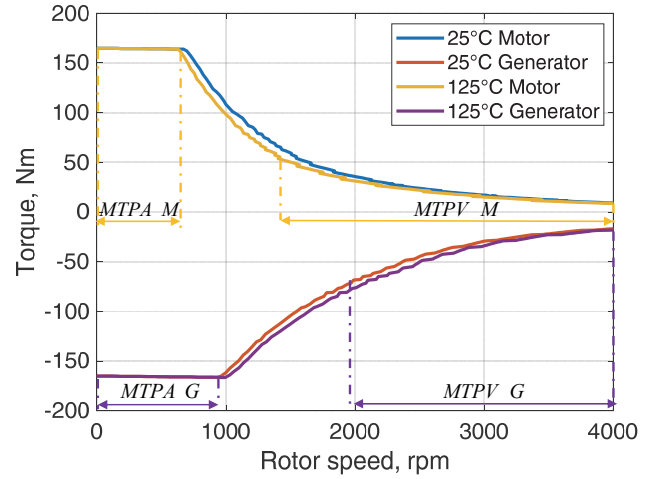


Fig. 7: Example of MTPS profiles computed at different stator and rotor temperatures ($\theta_s = \theta_r$) and fixed maximum voltage ($V_{\max} = 250\text{V}$).

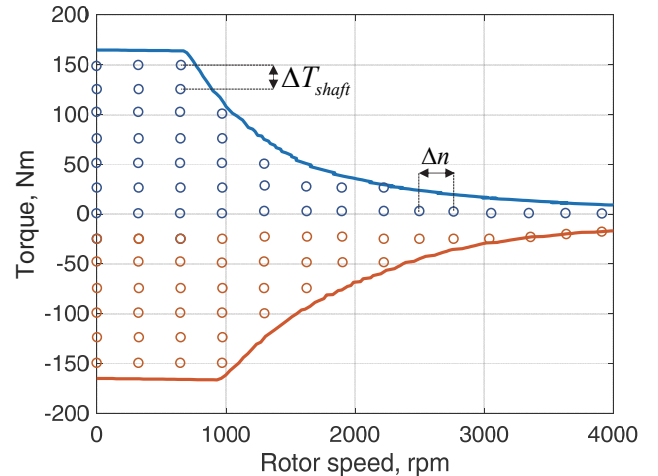


Fig. 8: Example of an efficiency map point (maximum voltage of 250 V, stator and rotor temperatures of 25 °C) for defined MTPS profiles in motor and generator operations.

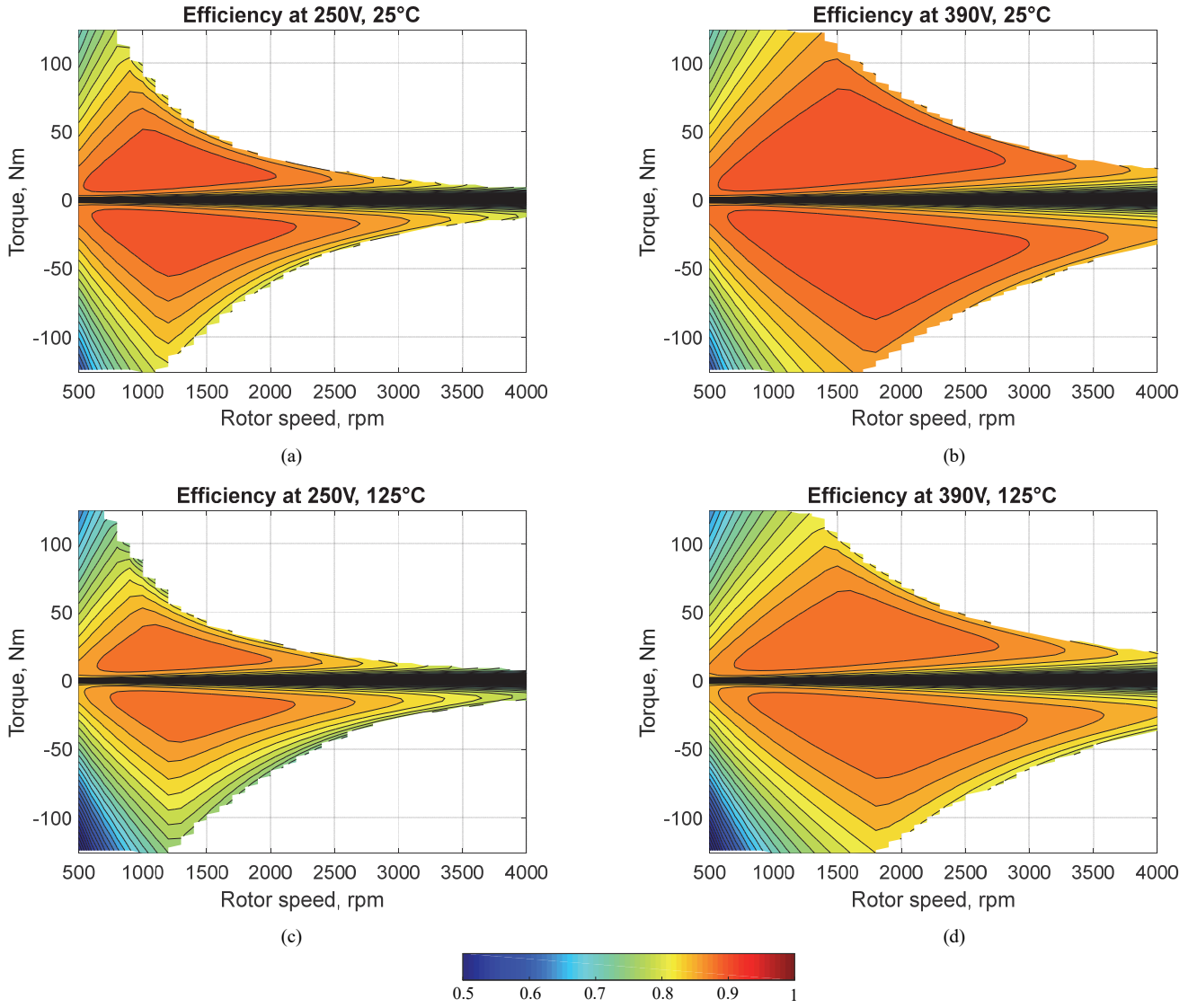


Fig. 9: Example of efficiency maps for different maximum line-to-line rms voltages and temperatures using the maximum efficiency strategy.

E. Step 5: IM Efficiency Mapping

For each point of the torque-speed map, the electromagnetic torque can be provided by different $(I_{eq,d}, I_{ed,q})$ combinations.

Depending on the final application, different criteria can be assumed to select the most convenient current components. Among them, it is worth mentioning the control strategies that maximize the machine efficiency, or those which minimize the stator Joule losses minimizing the absorbed stator current. Obviously, for each working point, the power supply system applies at the machine terminals a voltage level that depends on the considered supply strategy.

For this purpose, the developed mapping algorithm computes for each working point the motor loss components. In detail, the Joule losses for a three-phase machine are computed by the well-known equation in (15), where I_s and $I_{s,q}$ are peak values.

$$P_J = \frac{3}{2} \cdot R_s(\theta_s) \cdot I_s^2 + \frac{3}{2} \cdot R_r(\theta_r) \cdot k_r^2 \cdot I_{s,q}^2 \quad (15)$$

The iron losses are computed by (16), where R_{Fe} in function of the stator voltage and supply frequency could be determined experimentally (see Fig. 2) or estimated analytically, and E_s corresponds to the back-emf voltage applied at the iron resistance terminals and computed by (11).

$$P_{Fe} = \frac{3}{2} \cdot \frac{E_s^2}{R_{Fe}(V_s, f)} \quad (16)$$

The friction & windage losses P_{fw} are obtained by (17), where T_{fw} for the different rotational speeds has been determined experimentally (see Fig. 4)

$$P_{fw} = T_{fw} \cdot \omega_r \quad (17)$$

Finally, in the developed mapping algorithm, the total IM losses are computed by (18), where the additional stray load loss component P_{SLL} are assumed negligible for the present case of study.

$$P_{loss,tot} = P_J + P_{Fe} + P_l + P_{SLL} \quad (18)$$

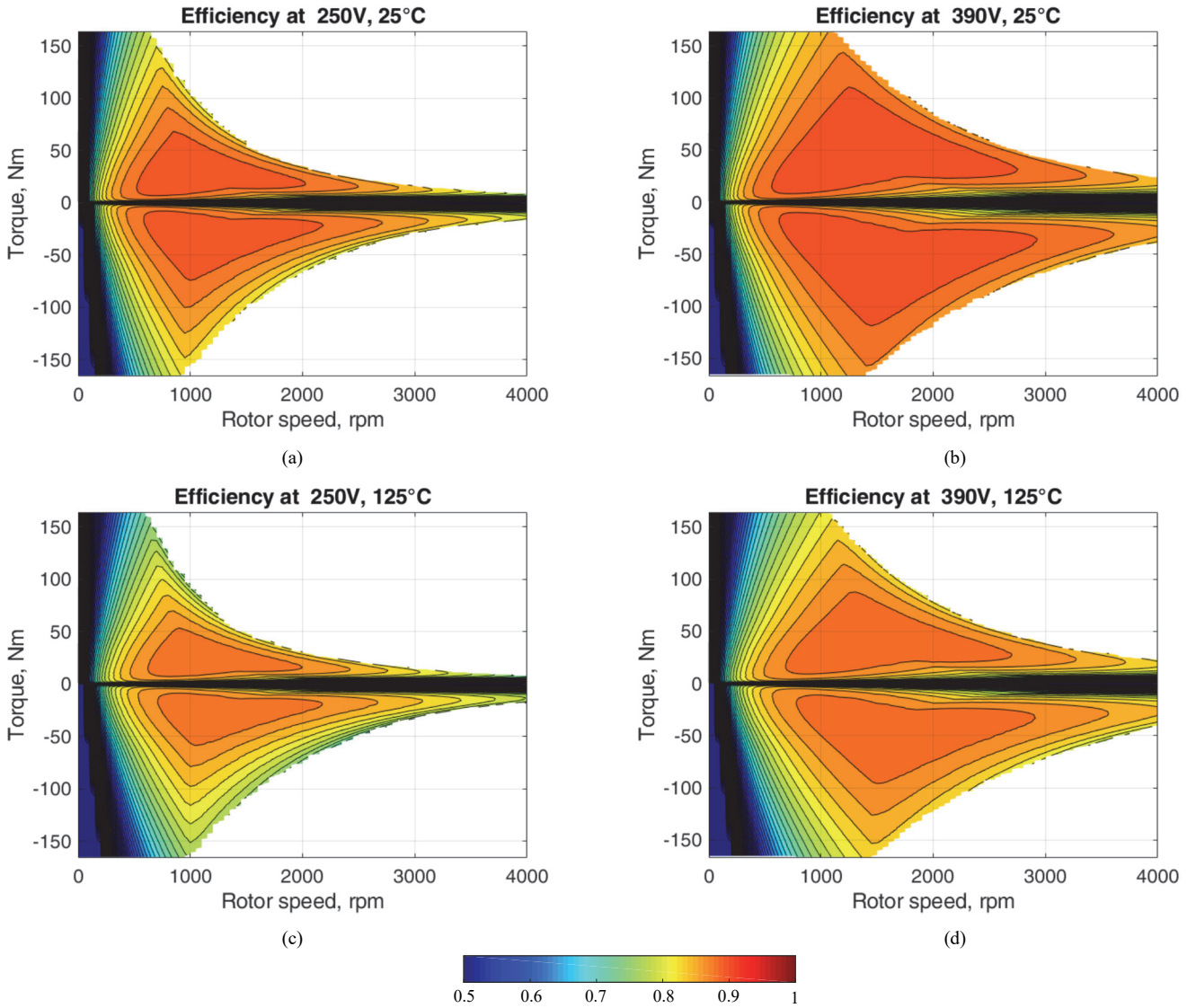


Fig. 10: Example of efficiency maps for maximum line-to-line rms voltages and temperatures using the minimum Joule losses strategy.

Therefore, if the selected IM supply strategy consists on the efficiency maximization, the mapping algorithm selects for each working point the (d,q) current components that minimize the overall losses computed by (18). Otherwise, if the supply strategy aims at minimizing the stator Joule losses, the algorithm selects the current components that minimize (15).

V. COMPUTED EFFICIENCY MAPS OF THE TESTED MOTOR

The mapping algorithm provides in output a set of efficiency maps in the torque-speed plane, computed for each combination of maximum available rms voltage and operating temperature considered for the analyses. In Fig. 9 are reported some example of maps computed for the motor under test when a supply strategy that maximize the machine efficiency is considered. Similarly, Fig. 10 shows the efficiency maps computed considering supply strategy that minimize the machine stator Joule losses.

It has been verified that the two considered supply strategies do not present significant differences in terms of efficiency because the IM under test is an industrial TEFC motor with relative low iron losses (with respect to the stator and rotor Joule losses), especially in overloaded conditions.

In any case, it was found that the adopted algorithm is able to discriminate between the two control strategies. In particular, for the same operation point, the efficiency results are slightly higher in the maximum efficiency control (Fig. 9) with respect to the minimum Joule loss strategy – see Fig. 10. As expected, the obtained maps significantly depend on the maximum available voltage; indeed, for higher voltage levels, the flux weakening operation starts for high-speed values, thus extending the constant torque region. Also, the results show the effect of the temperature on the machine losses, where higher working temperatures affect the machine efficiency negatively.

VI. EXPERIMENTAL VALIDATIONS

For the validation of the proposed mapping algorithm, the induction motor under test has been mounted on a test rig in order to measure its efficiency in different working points (see Fig. 11).

The rotor shaft has been coupled to a driving machine acting as a prime mover. Besides, the torque and the speed has been measured with a shaft transducer, allowing the direct method efficiency measurements, also known as the input-output method.

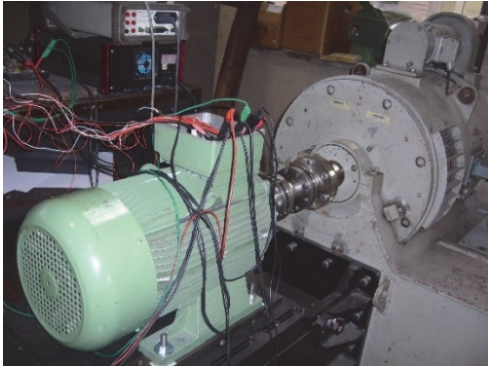


Fig. 11: Induction motor under test during the efficiency measurement in load conditions for the validation of the proposed mapping approach.

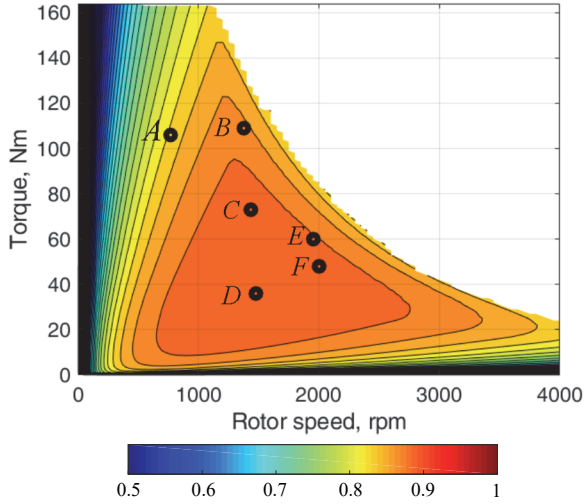


Fig. 12: Computed efficiency map and tested points for a stator temperature of 100 °C and a maximum rated voltage of 230 V (delta connection).

The used PWM power converter is fed by a dc source of 560 V. The switching frequency has been set at 4 kHz. The machine has been tested with a constant stator temperature of 100 °C. The validation of the proposed mapping algorithm has been performed by testing six operating points with motor in delta-connection, as shown in Fig. 11 and summarized in Table III and Table IV. It is noted that the values of the estimated quantities well agree with the measured one, providing the preliminary validation of the proposed algorithm. In particular, on the authors' opinion, the obtained results can be reasonably considered as one of the best approximation obtainable with off-line measurement approaches. Some discrepancies in the efficiency estimations could be attributed to the determination of the parameters with sinusoidal *ac* standard tests, while the load tests for efficiency measurements have been done under PWM supply.

VII. CONCLUSION

In this paper, an off-line approach for computing the efficiency maps of an induction machine operating in a wide torque-speed range has been presented. The efficiency mapping is based on an analytic model (i.e. the well-know equivalent circuit), whose parameters are adapted to the considered working point. In particular, in the presented case of study the parameter variations have been measured through the standard no-load and locked-rotor tests performed at different frequencies and voltage levels. However, the proposed approach can be implemented also deriving the machine parameters by analytical or FEM-based computations.

TABLE III
ESTIMATED AND MEASURED STATOR CURRENTS

Test point	Speed	Torque	Rms voltage	Stator current, A_{rms}	
				Algorithm	Measured
A	769 rpm	106 Nm	137	59.7	59.1
B	1377 rpm	109 Nm	229	61.2	59.3
C	1435 rpm	73 Nm	231	40.1	38.7
D	1477 rpm	36 Nm	232	23.9	23.1
E	1954 rpm	60 Nm	230	48.4	49.2
F	2002 rpm	48 Nm	231	35.4	35.0

(*) Line-to-line fundamental component of the PWM voltage.

TABLE IV
ESTIMATED AND MEASURED EFFICIENCIES

Test point	Efficiency		Error
	Algorithm	Measured	
A	76.0 %	74.0 %	2.00 %
B	89.7 %	89.3 %	0.45 %
C	87.3 %	87.0 %	0.34 %
D	82.9 %	82.3 %	0.73 %
E	83.0 %	81.2 %	2.80 %
F	83.7 %	79.0 %	3.15 %

The developed IM efficiency mapping features short computational time, considering different frequencies and voltage levels without knowing the machine design data. Also different control strategies and reference temperatures can be easily taken into account. Last but not least, the off-line algorithm provides the optimal current values for the control of the electric drives.

REFERENCES

- [1] A.M. EL-Refai, "Toward a Sustainable More Electrified Future – The role of electrical machines and drives", IEEE Electrification Mag., Vol. 7, No. 1, 2019.
- [2] S.S. Williamson, A. Emadi, K. Rajashekara, "Comprehensive Efficiency Modeling of Electric Traction Motor Drives for Hybrid Electric Vehicle Propulsion Applications", IEEE Trans. Vehicular Tech., Vol. 56, No. 4, 2007.
- [3] P.J. Ansell, K.S. Haran, "Electrified Airplanes: A path to zero-emission air travel", IEEE Electrification Mag., Vol. 8, No. 2, Jun.2020, pp. 18-26.
- [4] M. Bellone, M. Lundh, M. Wahde, S. MacKinnon, "Electrification and Automation in Maritime Applications – Employing AI techniques for energy optimization and efficiency", IEEE Electrification Mag., Vol. 7, No. 4, 2019, p.22-31.
- [5] Q. Zhang, N. Cui, K. Li, Y. Shang, C. Zhang, "Co-simulation of energy management strategy for hybrid electric vehicle in AVL InMotion", Chinese Automation Congress (CAC), 2017, pp. 4932-4937.
- [6] V. Groza, C.D. Pitis, A. Merabet, V.D. Giurgiu, "Novel Method of Pre-determining Induction Machine Parameters and Energetic Efficiency", 2013 IEEE Electrical Power & Energy Conference, pp. 1-6.
- [7] K. Li, S. Cui, A. Bouscayro, M. Hecquet, "Analytical Derivation of Efficiency Map of an Induction Machine for Electric Vehicle Applications", 2018 IEEE Vehicle Power and Propulsion Conference (VPPC), pp. 1-6.
- [8] A. Mahmoudi, W.L. Soong, G. Pellegrino, E. Armando, "Loss Function Modeling of Efficiency Maps of Electrical Machines", IEEE Trans. Ind. Appl., Vol. 53, No. 5, Sept./Oct. 2017, pp. 4221-4231.
- [9] Chu, Z. Zhu, J. Zhang, X. Liu, D. Stone, and M. Foster, "Investigation on operational envelopes and efficiency maps of electrically excited machines for electrical vehicle applications," IEEE Trans. Magnetics, vol. 51, pp. 1-10, 2015.
- [10] L. Alberti, N. Bianchi, and S. Bolognani, "Variable-speed induction machine performance computed using finite-element", IEEE Trans. Ind. Appl., Vol. 47, No. 2, March 2011, pp. 789-797.
- [11] International Standard IEEE 112, "Test Procedure for Polyphase Induction Motors and Generators", 2017.
- [12] Int. Standard IEC 60034-2-1, "Rotating Electric Machines Part 2-1: Standard methods for determining losses and efficiency from tests", 2015.
- [13] L. Alberti, N. Bianchi, S. Bolognani, "Field oriented control of induction motor: A direct analysis using finite element," in IEEE-IECON, 2008, pp. 1206-1209.
- [14] M. Carbonieri, N. Bianchi and L. Alberti, "Induction Motor Mapping Using Rotor Field-Oriented Analysis Technique," IEEE ECCE'2019, pp. 2321-2328.
- [15] A. Sterneck, O. Biro, K. Preis, S. Rainer, K. Kriskan, G. Ofner, "Calculation of load-dependent equivalent circuit parameters of squirrel cage induction motors using time-harmonic fem", ICEM' 2008, pp. 1-6
- [16] G. R. Slemon, "Modelling of induction machines for electric drives", IEEE Trans. Ind. Appl., Vol. 25, No. 6, pp. 1126- 1131, Nov 1989.
- [17] A. Boglietti, R. Bojoi, A. Cavagnino, M. Lazzari, "Core loss estimation method for PWM inverter fed induction motors," IECON 2010, pp. 811-816.